GEOPHYSICS, VOL. 85, NO. 3 (MAY-JUNE 2020); P. J33–J49, 15 FIGS., 2 TABLES.
10.1190/GEO2019-0244.1

Sparse magnetic vector inversion in spherical coordinates

Dominique Fournier[1], Lindsey J. Heagy[2], and Douglas W. Oldenburg[1]

ABSTRACT

Magnetic vector inversion (MVI) has received considerable attention over recent years for processing magnetic field data that are affected by remanent magnetization. However, the magnetization models obtained with current inversion algorithms are generally too smooth to be easily interpreted geologically. To address this, we have reviewed the MVI formulated in a spherical coordinate system. We tackle convergence issues posed by the nonlinear transformation from Cartesian to spherical coordinates by using an iterative sensitivity weighting approach and a scaling of the spherical parameters. The spherical formulation allows us to impose sparsity assumptions on the magnitude and direction of magnetization independently and, as a result, the inversion recovers simpler and more coherent magnetization orientations. The numerical implementation of our algorithm on large-scale problems is facilitated by discretizing the forward problem using tiled octree meshes. All of our results are generated using the open-source SimPEG software. We determine the enhanced capabilities of our algorithm on a large airborne magnetic survey collected over the Kevitsa Ni-Cu-platinum group elements (PGE) deposit. The recovered magnetization direction inside the ultramafic intrusion and in the host stratigraphy is consistent with laboratory measurements and provides evidence for tectonic deformation.

INTRODUCTION

The study of magnetism in rocks has a long history in earth sciences and continues to play a key role in mineral exploration and tectonic studies (Kissel and Laj, 1989; Pueyo et al., 2016; Li et al., 2019). Magnetic susceptibility, the ability of rocks to become magnetized by the geomagnetic field, is a useful property for mapping geology under cover. To this end, a large number of data sets, from global satellite measurements to deposit scale surveys, have been made available over the years. These data sets have also brought to light the prevalence of remanent magnetization: a permanent magnetization direction acquired by certain minerals and often associated with mineral deposits such as diamondiferous kimberlites, volcanogenic massive sulfides, and porphyry deposits (Henkel, 1991; Enkin, 2014). The remanent component of magnetization is typically ignored in the interpretation of magnetic data; therefore, it is often considered as "noise" that complicates the geologic interpretation.

Meanwhile, the same remanent component has been used extensively for paleomagnetic studies and regarded as meaningful geophysical "data." Several researchers have used the permanent magnetization orientation to map continental block rotation (Norris and Black, 1961; Vine and Matthews, 1963; Kissel and Laj, 1989), for fold and thrust belt reconstruction (Ramon et al., 2012) and in geochronology (Henkel, 1991; Enkin, 2003; Lockhart et al., 2004). Although these studies provide valuable information about earth's history, they have relied primarily on laboratory measurements performed on oriented cores. Analysis based on point measurements of magnetization direction remains a limiting factor in understanding the spatial and temporal variability of large fold and thrust belts systems (Pueyo et al., 2016).

Geophysical inversions provide an approach for extracting information about magnetization and constructing a 3D model of the subsurface from observed total magnetic field intensity (TMI) data. Imaging the shape and depth of magnetic bodies can help to identify mineral deposits, while recovering the orientation of magnetization can benefit paleomagnetic studies. As noted in the review by Li (2017), inversion strategies for magnetic data put forward in the literature can be broadly grouped into three main categories. In the first group, the magnetization orientation of compact bodies is estimated through search algorithms (Fedi et al., 1994; Dannemiller and Li, 2006), magnetic moment analysis (Helbig, 1963; Phillips, 2008), and inversion methods. The most common inversion approach uses simple parametric shapes to approximate elongated and

Manuscript received by the Editor 24 April 2019; revised manuscript received 11 January 2020; published ahead of production 11 February 2020; published online 19 March 2020.
[1]University of British Columbia, Geophysical Inversion Facility, Department of Earth, Ocean, and Atmospheric Sciences, Vancouver, British Columbia, Canada. E-mail: dfournie@eoas.ubc.ca (corresponding author); doug@eoas.ubc.ca.
[2]The University of California, Department of Statistics, Berkeley, California, USA. E-mail: lheady@berkeley.edu.

tabular bodies (Foss and McKenzie, 2011; Fullagar and Pears, 2013; Clark, 2014; Pratt et al., 2014). These methods are computationally inexpensive and work well when the magnetic response can be isolated, but, in practice, they rely heavily on experts to build and test different scenarios; this can become impractical in complex geologic settings.

The second group deals with remanence by transforming the field data into a quantity that is weakly sensitive to the orientation of magnetization. Magnetic amplitude data, for example, can be inverted for an effective susceptibility model; this approach was first introduced by Shearer (2005, p. 52). Although the amplitude inversion method has proven to be successful in identifying geologic features (Krahenbuhl and Li, 2007; Li et al., 2010), several drawbacks persist. First, the amplitude data must be calculated by preprocessing the observed TMI data either through a Fourier transform or by the equivalent source method (Li et al., 2014). This process may introduce unintended biases or numerical errors into the inversion. Second, the solution does not provide information about the direction of magnetization unless estimated in postprocessing. Third, the conversion to amplitude removes phase information from the data. This makes dip interpretation more difficult.

The third category, which is the focus of this study, aims to recover a 3D distribution of magnetization vectors directly from TMI data. Lelievre and Oldenburg (2009) introduce a magnetic vector inversion (MVI) algorithm, implemented in Cartesian (MVI-C) and spherical (MVI-S) coordinate systems. The MVI-C formulation is closely related to the method proposed by Kubota and Uchiyama (2005), and later adopted by Ellis et al. (2012). This has substantially improved the interpretation of magnetic data, and it is now frequently used in industry. Solving for a vector model remains difficult however because it results in a large underdetermined inverse problem with three times the number of variables (i.e., spatial components) compared with conventional inversions. The method relies heavily on the regularization function and often yields a smooth model that is too blurred for direct geologic interpretation. To deal with this deficiency, Li and Sun (2016) introduce a fuzzy c-means clustering technique to force the magnetization to be in a set number of domains. Sparsity constraints on the vector components have been proposed, either directly applied to the Cartesian components through Gramian constraints (Zhu et al., 2015) or indirectly through a cooperative approach (Fournier, 2015, p. 101; Liu et al., 2015). These "focusing" methods have shown success in better recovering the shape of compact bodies, but ambiguity remains about the magnetization direction.

Lelievre and Oldenburg (2009) advocate the use of the spherical representation so that constraints can be applied independently on the amplitude and orientation angles. This formulation is well-suited for incorporating sparsity and physical property constraints, but its implementation remains challenging. The nonlinear transformation makes the inversion prone to converge to a local minimum. The main reason is that the inversion parameters have different units (length, radian) and their respective sensitivities vary over several orders of magnitude. This issue has partially been addressed in Liu et al. (2017) with a fixed scaling parameter.

In this study, we propose to address the current limitations encountered with the MVI-S algorithm. Building upon the work of Liu et al. (2017), we define two scaling mechanisms: The first addresses the differing magnitudes of parameters in spherical coordinates, and the second compensates for rapid changes in the sensitivity due to the nonlinearity of the problem. We demonstrate the benefit of our iterative sensitivity reweighting strategy on a simple two-parameter problem. Using a stable MVI-S algorithm allows us to impose penalties on the magnetization direction and amplitude independently, which allows us to recover compact bodies with coherent magnetization direction. We use a tiled octree mesh decoupling approach to deal with the large memory footprint of the problem; this removes the need for compression. We first showcase our approach on a synthetic block model. The same algorithm is applied to an airborne magnetic field data set acquired over the Kevitsa Ni-Cu-platinum group elements (PGE) deposit, Finland. We unravel the complex magnetic signal to recover geologic units and their magnetization directions, and we recover regions of high magnetization at depth, which are in good agreement with known dunite units. The orientation of magnetization is consistent with previously published measurements performed on core samples. We infer tectonic deformation from the orientation of magnetization recovered within the folded host stratigraphy.

METHODOLOGY

Our goal is to image the subsurface using magnetic field data. From Gauss's law, the forward relation between the magnetization and the magnetic field response can be expressed as

$$\mathbf{b}(r) = \frac{\mu_0}{4\pi}\int_V \nabla\nabla\frac{1}{r}\cdot\mathbf{M}dV, \tag{1}$$

where $\mathbf{b}$ is the magnetic flux density in teslas (T) and r is the radial distance between an arbitrary position and the magnetic source with magnetization per unit volume $\mathbf{M}$ (A/m). For most geophysical applications, we do not measure the vector field $\mathbf{b}$ of magnetized bodies, but rather the amplitude of the field, or TMI data, that includes the geomagnetic and secondary fields

$$b^{\mathrm{TMI}} = \|\mathbf{b}_0 + \mathbf{b}\|, \tag{2}$$

where $\mathbf{b}_0 = \mu_0\mathbf{h}_0$ is the geomagnetic flux density. The anomalous field data d^{TMA} are computed by subtracting $\|\mathbf{b}_0\|$ from the TMI data. Thus,

$$d^{\mathrm{TMA}} = \|\mathbf{b}_0 + \mathbf{b}\| - \|\mathbf{b}_0\| \quad \approx \mathbf{b}\cdot\hat{b}_0. \tag{3}$$

This approximation is valid so long as $\|\mathbf{b}\| \ll \|\mathbf{b}_0\|$. In matter, the total magnetization per unit volume can be separated into its induced and remanent components such that

$$\mathbf{M} = \kappa(\mathbf{h}_0 + \mathbf{h}_s) + \mathbf{M}_r, \tag{4}$$

where the magnetic susceptibility κ (SI) is the physical property describing the ability of a rock to get magnetized under an applied field. In nature, this inducing field has two components: the earth's geomagnetic field $\mathbf{h}_0$ and secondary fields $\mathbf{h}_s$ related to local magnetic anomalies. The remanent magnetization $\mathbf{M}_r$ is a permanent magnetization preserved in the absence of an inducing field. This is the quantity of interest in the field of paleomagnetism as it preserves information about the inducing field direction and position of a rock at the time of remanence acquisition.

Our goal is to recover a 3D model m describing some quantity related to magnetization ($m := \mathbf{M}$) from the observed data. The inverse problem can be formulated as an optimization problem of the form (Tikhonov et al., 1995, p. 7)

DOI:10.1190/geo2019-0244.1

$$\min_m \phi(m) = \phi_d + \beta\phi_m \quad \text{subject to } \phi_d \le \phi_d^*. \tag{5}$$

The objective function $\phi(m)$ has two terms. The misfit function,

$$\phi_d = \sum_{i=1}^{N}\left(\frac{d_i^{\text{pre}} - d_i^{\text{obs}}}{\sigma_i}\right)^2, \tag{6}$$

measures the residual between the predicted data $d^{\text{pre}} = F[m]$ and observed d^{obs} data normalized by estimated uncertainties σ. Assuming that the noise and error on the data are random, our expected target misfit $\phi_d^* = N$, where N is the number of data. The model objective function ϕ_m also known as the regularization function is typically made up of several functions that control the magnitude and roughness of the model. The trade-off parameter β controls the relative importance between the two competing objectives. In this research, we use the general l_p-norm measure of the model and its spatial gradients as our model objective function:

$$\phi_m = \sum_{r=s,x,y,z} \alpha_j \int_V w_r |f_r(m)|^{p_r} dV. \tag{7}$$

The regularization functions f_r are user-defined but most often have the following form:

$$f_s = m, \quad f_x = \frac{dm}{dx}, \quad f_y = \frac{dm}{dy}, \quad f_z = \frac{dm}{dz}. \tag{8}$$

Thus, $f_s(m)$ measures the size of m and $f_x(m)$, $f_y(m)$, and $f_z(m)$ measure the roughness along orthogonal directions. These functionals can also include a reference model m_{ref}, but for the sake of notation we set it to zero. Weighting terms w_r allow the user to adjust the strength of the regularization function in specific regions of the inversion domain.

The general strategy to minimize equation 5 requires that we discretize the model onto a mesh (we use $\mathbf{m}$ to denote the discretized model which has length M) and find a solution such that the gradient of the objective function

$$\begin{aligned}\mathbf{g} = \nabla_m\phi(\mathbf{m}) = \nabla_m\phi_d + \beta[\alpha_s\nabla_m\phi_s + \alpha_x\nabla_m\phi_x \\ + \alpha_y\nabla_m\phi_y + \alpha_z\nabla_m\phi_z] = \mathbf{0}.\end{aligned} \tag{9}$$

A solution to the optimization (equation 5) is found for decreasing values of the trade-off parameter β; we stop when we find a suitable model that reproduces the data to within a predefined tolerance:

$$\frac{|\phi_d - \phi_d^*|}{\phi_d^*} \le \eta_{\phi_d}. \tag{10}$$

Building upon the work presented in Fournier and Oldenburg (2019), we solve the nonlinear problem in equation 7 by the scaled iteratively reweighted least-squares (S-IRLS) method. The ℓ_p-norm is approximated by the Lawson method, such that equation 7 is expressed as a weighted least-squares regularization of the form

$$\phi_r^{p_r} = \sum_j^M \frac{f_{r_j}^2}{((f_{r_j}^{(k-1)})^2 + \epsilon_r^2)^{1-p_r/2}} w_j, \tag{11}$$

where k denotes the iteration number and the subscript r is one of the functions making up the regularization (e.g., s, x, y, and z). The regularization function in equation 12 allows for the independent mixing of norms on the complete interval $0 \le p_r \le 2$. This lets us generate a suite of models with different characteristics and assess the variability of the solution by varying the p_r parameters. For small p_s values, the inversion favors compact anomalies with large physical property contrasts while reducing the p_{xyz} values generate flat anomalies with sharp edges along the Cartesian directions. This formulation greatly increases the flexibility of inversion outcomes compared with those using conventional ℓ_2-norm measures.

We express the regularization function equation 7 in matrix form as

$$\phi_m = \sum_{r=s,x,y,z} \alpha_r \|\mathbf{W}_r\mathbf{R}_r\mathbf{D}_r\mathbf{m}\|_2^2, \tag{12}$$

where the gradient terms $\mathbf{D}_x, \mathbf{D}_y$, and $\mathbf{D}_z$ are the finite-difference operators measuring the model roughness along the three Cartesian directions and $\mathbf{D}_s$ is the identity matrix. Once again, each term may, or may not, include a reference model $\mathbf{m}_{\text{ref}}$. Hyperparameters α_r allow the user to change the relative influence of each term. In this study, we set $\alpha_r = 1$ for simplicity. Sparsity weights $\mathbf{R}_r$ are the discretized version of equation 11 and are calculated as

$$\mathbf{R}_r = \text{diag}[\gamma_r(\mathbf{D}_r(\mathbf{m}^{(k-1)})^2 + \epsilon_r^2)^{-(1-p_r/2)}]^{1/2} \tag{13}$$

such that weights depend on the model obtained at a previous kth iteration. The γ_r scaling parameters are used to balance the contribution of different ℓ_p-norms based on the maximum derivatives such that

$$\gamma_r = \frac{\|\mathbf{g}_r^2\|_\infty}{\|\mathbf{g}_r^{p_r}\|_\infty}. \tag{14}$$

In equation 14, the superscript denotes the p-value used to approximate the ℓ_p-norm used in equation 13. Our objective is to minimize equation 12 for $\epsilon_r \to 10^{-8}$, which we do along scaled gradient steps such that each regularization term ϕ_r remains influential throughout the iterative process. More details about the S-IRLS algorithm are provided in Fournier and Oldenburg (2019).

Finally, the sensitivity weighting functions $\mathbf{W}_r$ are used to counteract spatial changes in sensitivities; designing these weights is the main focus of this research. In the work of Li and Oldenburg (1996), a distance weighting function is used, and it is fixed at the onset. In this study, we advocate for an iterative reweighting strategy calculated directly from the sensitivity of a given problem. Adapted from Haber et al. (1997), we formulate the sensitivity-based weighting function:

$$\mathbf{W}_r = \mathbf{P}_C^{F_r}\text{diag}\left[\left[\frac{\mathbf{w}}{\max(\mathbf{w})}\right]^{1/2}\right], \quad w_j = \left[\sum_{i=1}^{N} J_{ij}^2 + \delta\right]^{1/2}, \tag{15}$$

where weights w_j measure the sum of squares of the columns of the sensitivity matrix

$$\mathbf{J} = \frac{\partial\mathbb{F}[\mathbf{m}^{(k)}]}{\partial\mathbf{m}}. \tag{16}$$

The projection matrices $\mathbf{P}_C^{F_r}$ average the sensitivity weights from cell center to corresponding faces (or the identity matrix for ϕ_s). A small constant δ is added to avoid singularity. This sensitivity weighting strategy is general and adaptable to any inverse problems in which the sensitivity matrix can be calculated explicitly. Although the initial purpose of the sensitivity weighting function of Li and Oldenburg (1996) is to counteract the decay of potential fields, we will show numerically that the iterative rescaling process can also be beneficial in improving the convergence of gradient methods applied to nonlinear inverse problems.

Susceptibility inversion

To illustrate some challenges that remanent magnetization can cause in magnetic inversions, we revisit the linear susceptibility method implemented by Li and Oldenburg (1996), Pilkington (1997), and others. As derived by Sharma (1966), the integral in equation 1 can be evaluated analytically for the magnetic field of a rectangular prism such that

$$F[m] = d^{\text{pre}} = \hat{\mathbf{b}}_0^{\text{T}}\mathbf{T}\mathbf{m}, \tag{17}$$

where the matrix $\mathbf{T} \in \mathbb{R}^{3\times3}$ describes the linear relation between the magnetic field components measured outside a discrete prism with magnetization $\mathbf{m} = [m_x, m_y, m_z]^{\text{T}}$. The dot product with the normalized inducing flux $\hat{\mathbf{b}}_0$ handles the total magnetic anomaly (TMA) projection. Different assumptions regarding the magnetization in equation 4 give rise to different inverse problems. We will assume here that the magnetic response is purely induced along earth's field and ignore remanent and self-demagnetization effects ($\mathbf{M}_r = \mathbf{h}_s = 0$). Under this assumption, the definition of magnetization equation 4 simplifies to

$$\mathbf{M} = \kappa\mathbf{h}_0. \tag{18}$$

This assumption gives rise to a linear system relating N data, $\mathbf{d}^{\text{pre}}$, to M discrete model cells of magnetic susceptibility $\boldsymbol{\kappa}$

$$\mathbf{d}^{\text{pre}} = \mathbf{F}\boldsymbol{\kappa} \quad \mathbf{d}^{\text{pre}} \in \mathbb{R}^N, \quad \mathbf{F} \in \mathbb{R}^{N\times M}, \quad \boldsymbol{\kappa} \in \mathbb{R}^M. \tag{19}$$

As an entry point to the inverse problem with remanent magnetism, we provide a synthetic experiment. From equation 19, we generate magnetic data on 441 stations on a 21×21 grid. The data are centered over a magnetized cube 25 m in width and placed 15 m below the grid (Figure 1a). The earth is discretized in 5 m cubic cells. The magnetization of the block is made up of an induced and a remanent component. We set the magnetic susceptibility of the cube to be $\kappa = 0.035$ SI and the inducing flux to be $\mathbf{b}_0$ [50,000 nT, I: 90°, D: 0°]. We set the remanent component equal in magnitude and pointing along the x-axis $\mathbf{M}_r$ [1.4 A/m, I: 0°, D: 90°]. This results in a total magnetization $\mathbf{M}$ [2.0 A/m, I: 45°, D: 90°] as shown in Figure 1b. From equation 19, we calculate the TMA data with random Gaussian noise added to simulate field conditions ($\sigma = 1$ nT).

Because we are dealing with strictly positive magnetic susceptibility κ, we impose bounds by the projected gradient method (Vogel, 2002, p. 157) and use a Gauss-Newton method to solve the inverse problem. A gradient descent direction $\delta\mathbf{m}$ is calculated by solving

$$\mathbf{H}\delta\mathbf{m} = -\mathbf{g}, \tag{20}$$

where $\mathbf{g}$ is the gradient in equation 9 of the objective function:

$$\mathbf{g} = \mathbf{J}^{\text{T}}\mathbf{W}_d^{\text{T}}\mathbf{W}_d(\mathbb{F}[\mathbf{m}^{(k-1)}] - \mathbf{d}^{\text{obs}}) + \beta \sum_{r=s,x,y,z} \alpha_r \mathbf{D}_r^{\text{T}}\mathbf{R}_r^{\text{T}}\mathbf{W}_r^{\text{T}}\mathbf{W}_r\mathbf{R}_r\mathbf{D}_r\mathbf{m}^{(k-1)}, \tag{21}$$

and $\mathbf{H}$ is the approximate Hessian:

$$\frac{\partial^2\phi}{\partial m^2} \approx \mathbf{H} = \mathbf{J}^{\text{T}}\mathbf{W}_d^{\text{T}}\mathbf{W}_d\mathbf{J} + \beta \sum_{r=s,x,y,z} \alpha_r \mathbf{D}_r^{\text{T}}\mathbf{R}_r^{\text{T}}\mathbf{W}_r^{\text{T}}\mathbf{W}_r\mathbf{R}_r\mathbf{D}_r. \tag{22}$$

We use the conjugate gradient method (Hestenes and Stiefel, 1952) to solve equation 20. The model update at the kth iteration is then given by

$$\mathbf{m}^{(k)} = \mathbf{m}^{(k-1)} + \alpha\delta\mathbf{m}, \tag{23}$$

where the step length α is found by a line-search method (Nocedal and Wright, 1999, p. 30). The optimization problem is solved for a sequence of β-values until the data misfit reaches the user-defined tolerance η_{ϕ_d} defined in equation 10. Because this problem is linear with respect to the model parameters, the sensitivity matrix simplifies to

$$\mathbf{J} = \frac{\partial\mathbb{F}[\boldsymbol{\kappa}]}{\partial\boldsymbol{\kappa}} = \mathbf{F} \tag{24}$$

and does not change as a function of iteration.

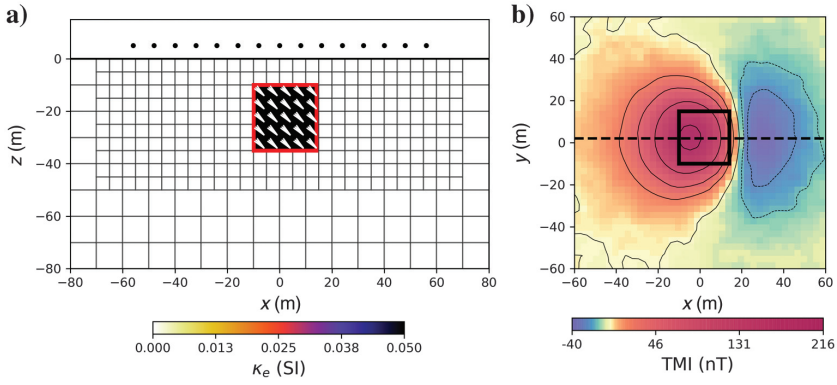

Figure 1. (a) Vertical section through the synthetic block model ($Y = 0$ m) with magnetization $\mathbf{M}$ [2.0 A/m, I:45°, D:90°] ($\kappa_e = 0.05$ SI). Survey points (the black dots) are placed 15 m above the magnetic anomaly. (b) Simulated TMI data map with random Gaussian noise added, 1 nT standard deviation. The horizontal position of the block is shown in black for reference.

We begin with the conventional approach that assumes a smooth model (p_s, p_x, p_y, and $p_z = 2$). After reaching the target misfit criteria in equation 10, we recover the susceptibility model shown in Figure 2a. We note that the position of the susceptibility anomaly is shifted to the side of the true block and appears to dip at 45° angle toward the west. This is due to the large negative lobe introduced in the data by the remanent component that we have ignored. Attempting to improve the solution by solving for a sparse model (p_s, p_x, p_y, and $p_z = 0$) yields the solution presented in Figure 2b. The magnetic anomaly is imaged at the right depth, and the vertical extent is better recovered, but the position and shape of the anomaly have not improved. In both cases, the data residual maps (Figure 2c and 2d) show correlated signal with the location of negative data. The inversion has difficulty in reproducing the negative anomalies using strictly positive susceptibility subject to a vertical inducing field.

The presence of remanence has long been recognized as an obstacle for the geologic interpretation of magnetic data. In a mining exploration context, having the wrong image could result in false drilling targets, which is costly in time, resources, and confidence in geophysical methods. These factors motivate the need for a more robust algorithm that does not require knowledge about the orientation of magnetization.

MVI-C parameters

Generalizing the susceptibility inversion, Lelievre and Oldenburg (2009) propose a strategy to directly recover the magnetization vector without assumptions about the orientation. They define an effective susceptibility parameter that scales the strength of magnetization along orthogonal directions such that

$$\boldsymbol{\kappa}_e = \frac{\mathbf{M}}{\|\mathbf{h}_0\|}. \tag{25}$$

Rewriting the discrete system in equation 19 in terms of three orthogonal components of magnetization (u, v, w), we obtain the augmented system

$$\mathbf{d}^{\text{pre}} = \mathbf{F}_e\boldsymbol{\kappa}_e \quad = [\mathbf{F}_u\mathbf{F}_v\mathbf{F}_w]\begin{bmatrix}\boldsymbol{\kappa}_u\\ \boldsymbol{\kappa}_v\\ \boldsymbol{\kappa}_w\end{bmatrix} \quad \mathbf{F}_u, \mathbf{F}_v, \mathbf{F}_w \in \mathbb{R}^{N\times M}, \tag{26}$$

where $\mathbf{F}_u$, $\mathbf{F}_v$, and $\mathbf{F}_w$ are the forward operators for the components of magnetization. We are now dealing with a linear system that has three times the number of unknown parameters compared to the susceptibility assumption ($\boldsymbol{\kappa}_e \in \mathbb{R}^{3M}$). The regularization function in equation 12 becomes

$$\phi_m = \sum_{c=u,v,w}\sum_{r=s,x,y,z}\alpha_{c_r}\|\mathbf{W}_r\mathbf{R}_{c_r}\mathbf{D}_{c_r}\mathbf{P}_c\boldsymbol{\kappa}_e\|_2^2, \tag{27}$$

where the projection matrices $\mathbf{P}_c$ select individual components of the vector model $\boldsymbol{\kappa}_e$. Our regularization is made up of 12 terms. Norm measures can be applied to each Cartesian component independently.

Keeping the same inversion methodology and smooth assumptions ($p_{c_s}, p_{c_x}, p_{c_y}, p_{c_z} = 2$), we recover the magnetization model presented in Figure 3a. This solution is an improvement over the susceptibility inversion as the bulk magnetization is recovered at the right position and with the correct magnetization orientation on average inside the block. However, we note that the solution is distributed over a large volume and with a broad distribution in magnetization direction.

To reduce the complexity of the solution, we once again resort to the ℓ_p-norm measure ($p_{c_s}, p_{c_x}, p_{c_y}, p_{c_z} = 0$). As shown in Figure 3b, the recovery of the block has clearly improved. It is

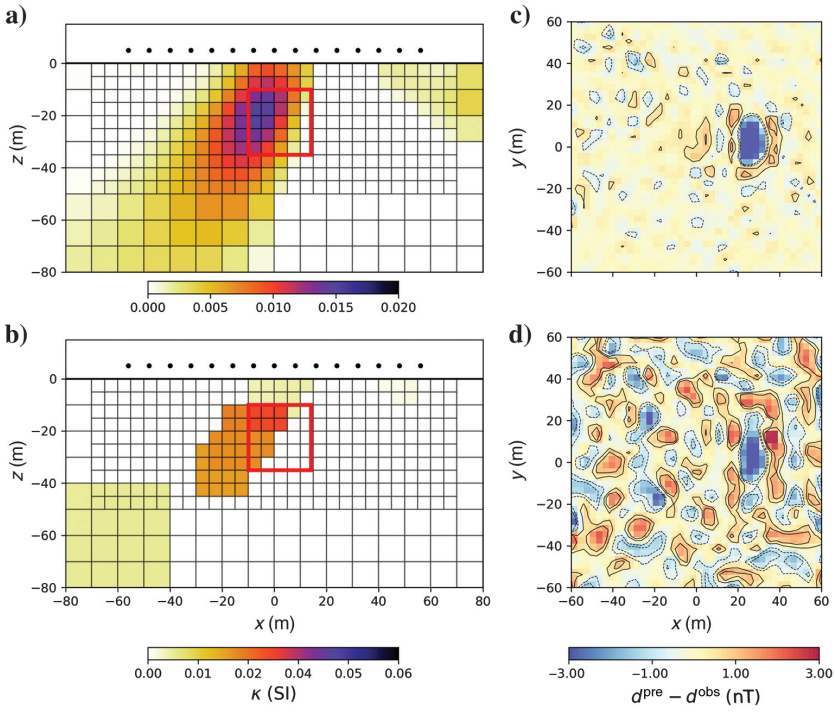

Figure 2. Vertical section through the recovered susceptibility model using (a) smooth assumption ($p_s, p_x, p_y, p_z = 2$) and (b) sparse ℓ_p-norms to recover a compact model ($p_s, p_x, p_y, p_z = 0$). Both solutions show an anomaly with a false dip due to the wrong assumption of a vertical magnetization. Data residuals for (c) the smooth and (d) compact solution show the correlated signal with the negative data.

important to point out, however, that the magnetization vectors are pointing along the Cartesian directions and the anomaly is slightly wider than the true model. In the Cartesian formulation, the direction and strength of magnetizations are coupled in the vector components. Therefore, this formulation lacks flexibility in recovering sparse vector along arbitrary orientations. This was the main motivation behind recent research investigating more advanced regularization methodologies (Fournier, 2015, p. 101; Liu et al., 2015; Zhu et al., 2015). We will attempt to improve this solution by decoupling the strength and direction of the magnetization vector with the spherical formulation.

MVI-S parameters

As an alternative to the Cartesian formulation, Lelievre and Oldenburg (2009) also propose the vector inversion in a spherical coordinate system. The conversion between Cartesian to spherical system follows the relation

$$u = \rho\ \cos(\theta)\cos(\phi) v = \rho\ \cos(\theta)\ \sin(\phi) w = \rho\ \sin(\theta), \tag{28}$$

where the magnetization vector is defined by parameters of amplitude (ρ) and two angles (θ, ϕ). The spherical formulation separates the magnitude and orientation of magnetization vector, which comes with two advantages. First, physical property constraints from rock measurements (Koenigsberger ratio and magnetization angle) can be easily incorporated. Second, sparsity constraints can be applied to the magnitude and orientation independently, potentially resulting in compact bodies with a uniform magnetization direction in any orientation.

Despite its obvious advantages, the MVI-S method has received little attention in the literature due to the nonlinear transformation it introduces. We demonstrate challenges encountered with the spherical approach on our synthetic problem. Taking the partial derivatives of equation 26 as a function of $\mathbf{m}(\boldsymbol{\rho}, \boldsymbol{\theta}, \boldsymbol{\phi})$ yields

$$\mathbf{J} = \frac{\partial \mathbf{F}_e[\boldsymbol{\kappa}_e]}{\partial \mathbf{m}} = \frac{\partial \mathbf{F}_e[\boldsymbol{\kappa}_e]}{\partial \boldsymbol{\kappa}_e}\frac{\partial \boldsymbol{\kappa}_e}{\partial \mathbf{m}}, \tag{29}$$

where $\partial \mathbf{k}_e / \partial \mathbf{m}$ involves partial derivatives of trigonometric functions prescribed in equation 28. The sensitivity matrix can be linearized before each Gauss-Newton step as

$$\mathbf{J} = \mathbf{F}_e \mathbf{S}, \tag{30}$$

where the matrix $\mathbf{S}$ holds the partial derivatives

$$\mathbf{S} = \begin{bmatrix} \cos\theta\cos\phi & -\rho\sin\theta\cos\phi & -\rho\cos\theta\sin\phi \\ \cos\theta\sin\phi & -\rho\sin\theta\sin\phi & \rho\cos\theta\cos\phi \\ \sin\theta & \rho\cos\theta & 0 \end{bmatrix}. \tag{31}$$

With this choice of parameterization, the regularization function becomes

$$\phi_m = \sum_{c=\rho,\theta,\phi} \sum_{r=s,x,y,z} \alpha_{c_r} \|\mathbf{W}_r \mathbf{R}_{c_r} \mathbf{D}_{c_r} \mathbf{P}_c \mathbf{m}\|_2^2. \tag{32}$$

We note that zero reference angle values $\boldsymbol{\theta}_{\text{ref}}$ and $\boldsymbol{\phi}_{\text{ref}}$ would imply a magnetization direction pointing along the x-axis. Because we do not want to assume a specific orientation (no ground truth), we set $\alpha_{\theta_s} = \alpha_{\phi_s} = 0$ in all our experiments such that the regularization only penalizes the change in angle between neighboring cells.

To demonstrate the difficulties that the nonlinearity of the MVI-S formulation can cause in the inversion, we invert our synthetic TMI data with the wrong initial assumption $\mathbf{m_0}(\rho = 10^{-2}, \theta = -45^{\circ}, \phi = 0^{\circ})$, such that the starting magnetization orientation is 90° from

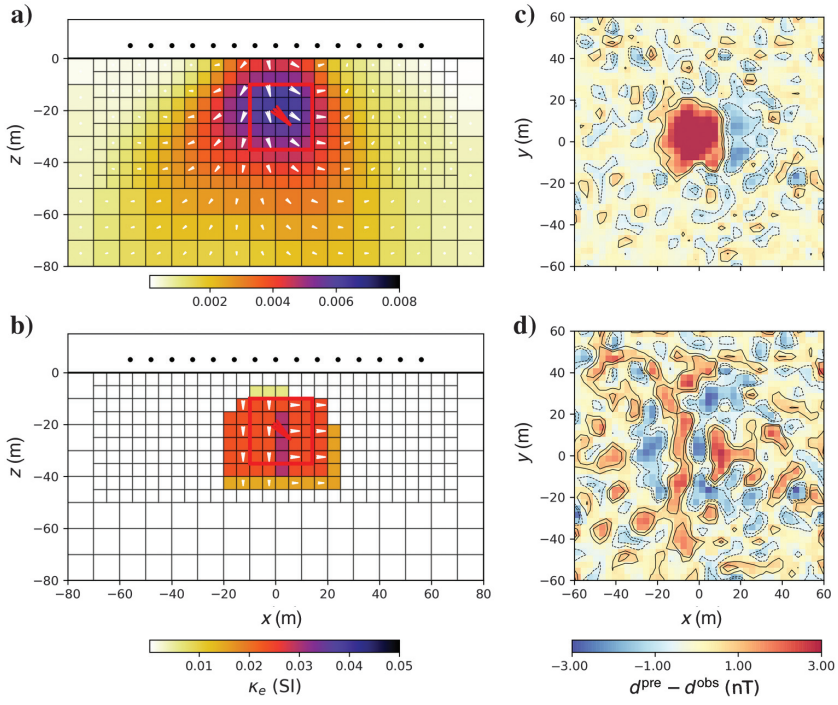

Figure 3. Vertical section through the recovered magnetization vector model using the Cartesian formulation with (a) smooth l_2-norm assumption and (b) sparsity constraints applied on all three Cartesian components ($p_{i_s}, p_{i_x}, p_{i_y}, p_{i_z} = 0$). The color is scaled by the magnitude of magnetization. The true magnetization direction is shown with a red arrow. Data residual map calculated with the (c) smooth and (d) compact solutions.

the true model (Figure 4a). After convergence of the algorithm, we recover the model shown in Figure 4b. The solution is a poor representation of the true magnetization. Model updates were forced to stop before reaching the target data misfit, and the optimization is likely trapped in a local minimum. We note that most of the model updates were performed on the amplitude ρ, with only marginal changes on the angle of magnetization. Similar behaviors have been documented by Lelievre and Oldenburg (2009) and later by Liu et al. (2017), who attributed the problem to an imbalance between the model parameters. Before attempting to implement more advanced constraints, we make improvements to the convergence of the nonlinear MVI-S formulation.

Iterative sensitivity reweighting

To gain some insight about the issues encountered with the MVI-S formulation, we consider a simpler two-parameter linear problem of the form

$$x + 2y = 1, \tag{33}$$

which we can express in matrix form as

$$\mathbf{F}_C\mathbf{m}_C = \mathbf{d}^{\text{obs}}, \quad \mathbf{F}_C = [12], \quad \mathbf{m}_C = \begin{bmatrix} x \\ y \end{bmatrix}, \quad \mathbf{d}^{\text{obs}} = 1. \tag{34}$$

This defines an underdetermined linear system of equations. Just as we did for the magnetic inverse problem, we can isolate a solution by minimizing an objective function of the form

$$\phi(m) = \|\mathbf{F}_C\mathbf{m}_C - \mathbf{d}^{\text{obs}}\|_2^2 + \beta_C\|\mathbf{m}_C\|_2^2. \tag{35}$$

Figure 5a displays a contour map of the objective function along with its gradients. Following the same methodology as shown in equation 9, we find a solution such that the gradient of the objective function $\phi(m)$ vanishes

$$\frac{\partial\phi}{\partial\mathbf{m}} = \mathbf{g} = (\mathbf{F}_C^{\text{T}}\mathbf{F}_C + \beta_C\mathbf{I})\mathbf{m}_C - \mathbf{F}_C^{\text{T}}\mathbf{d}^{\text{obs}} = \mathbf{0}, \tag{36}$$

where $\mathbf{I}$ is the identity matrix. The factor of 2 from the derivative of the ℓ_2-norm is absorbed by the zero on the right side. After determining a trade-off parameter β_C such that $\phi_d \leq 10^{-3}$, we recover the Cartesian model $\mathbf{m}_C[x = 0.2, y = 0.4]$. It is the solution that minimizes the distance (evaluated with the ℓ_2-norm) between the origin and the solution space of $\mathbf{F}_C$. We note that the relative magnitudes of model parameters in $\mathbf{m}_C$ reflect the size of the forward coefficients in $\mathbf{F}_C$.

As previously discussed for the magnetic problem, the smallest solution is often not satisfactory because it is strongly influenced by the physics of the experiment. From equation 15, we can introduce sensitivity-based weights to counteract this bias toward a large y value:

$$\mathbf{W}_C = \text{diag}\left[\left[\frac{\mathbf{w}_C}{\max(\mathbf{w}_C)}\right]^{1/2}\right], \quad w_{C_j} = \left[\sum_{i=1}^{N} F_{ij}^2\right]^{1/2}, \tag{37}$$

where $\mathbf{W}_C$ holds the sensitivity weights added to the regularization ($\mathbf{w}_C = [1, 2]^{\text{T}}$). The new weighted objective function becomes

$$\phi(m) = \|\mathbf{F}_C\mathbf{m}_C - \mathbf{d}^{\text{obs}}\|_2^2 + \beta_C\|\mathbf{W}_C\mathbf{m}_C\|_2^2, \tag{38}$$

and the weighted gradient is

$$\mathbf{g}_C = \mathbf{F}_C^{\text{T}}\mathbf{F}_C\mathbf{m}_C + \beta_C\mathbf{W}_C^{\text{T}}\mathbf{W}_C\mathbf{m}_C - \mathbf{F}_C^{\text{T}}\mathbf{d}^{\text{obs}}. \tag{39}$$

After determining the appropriate β_C^*, we get the solution $\mathbf{m}_C^*[x = 0.33, y = 0.33]$ marked with a black circle in Figure 5a. We have

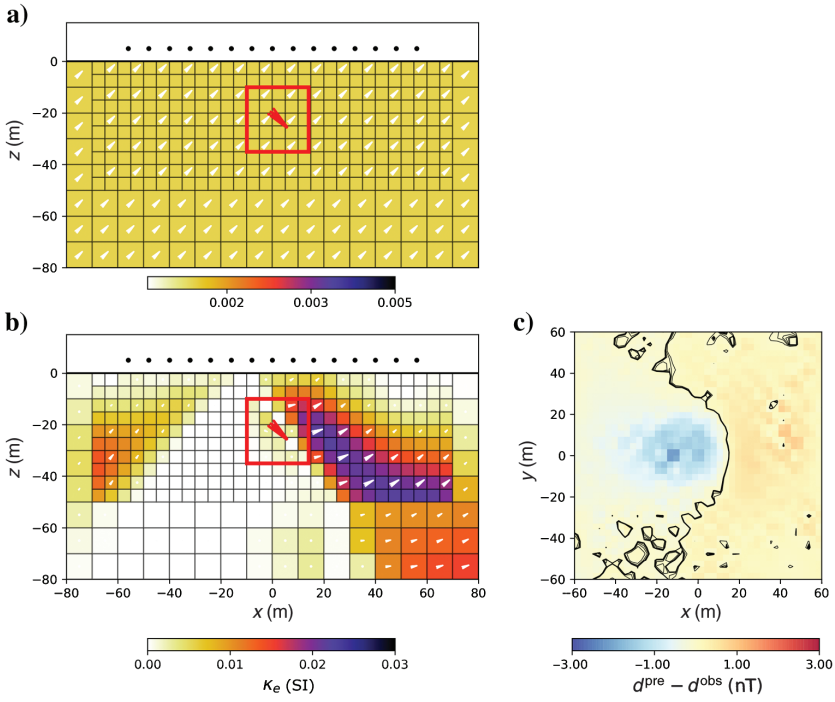

Figure 4. Vertical section through the (a) starting model and (b) recovered magnetization vector model in spherical coordinates with its (c) data residual map. The inversion stopped after three iterations, unable to further reduce the objective function.

reached the only solution with equal contribution from both model parameters that also predict the data within the tolerance.

Alternatively, we can attempt to solve the same problem in a polar coordinate system under the transformation

$$\mathbf{m}_P = [\rho, \theta]^{\mathrm{T}}, \quad x = \rho \cos\theta, \quad y = \rho \sin\theta, \tag{40}$$

where the polar model $\mathbf{m}_P$ is defined by a radius ρ and an angle θ. This is analogous to the spherical transformation performed for the MVI-S formulation in equation 28. The objective function to be minimized becomes

$$\phi(\mathbf{m}_P) = \|\mathbb{F}[\mathbf{m}_P] - \mathbf{d}^{\mathrm{obs}}\|_2^2 + \beta_P \|\mathbf{W}_C \mathbf{m}_P\|_2^2. \tag{41}$$

The inverse problem is now nonlinear with respect to the polar model, so we solve it iteratively with the standard Gauss-Newton procedure described in equation 20. The partial derivatives of the forward mapping with respect to the polar coordinates are calculated by

$$\mathbf{J} = \frac{\partial \mathbb{F}[\mathbf{m}_P]}{\partial \mathbf{m}_P} = \frac{\partial \mathbb{F}[\mathbf{m}_P]}{\partial \mathbf{m}_C} \frac{\partial \mathbf{m}_C}{\partial \mathbf{m}_P} = \mathbf{F}_C \mathbf{S}, \tag{42}$$

where the matrix $\mathbf{S}$ holds the partial derivatives of the model with respect to the polar parameters

$$\mathbf{S} = \begin{bmatrix} \cos\theta & -\rho \sin\theta \\ \sin\theta & \rho \cos\theta \end{bmatrix}. \tag{43}$$

The gradient of the objective function becomes

$$\mathbf{g}_P = \mathbf{S}^{\mathrm{T}} \mathbf{F}_C^{\mathrm{T}} \mathbb{F}[\mathbf{m}_P] + \beta_P \mathbf{W}_C^{\mathrm{T}} \mathbf{W}_C \mathbf{m}_P - \mathbf{S}^{\mathrm{T}} \mathbf{F}_C^{\mathrm{T}} \mathbf{d}^{\mathrm{obs}}. \tag{44}$$

A trade-off parameter β_P is determined through the cooling schedule established previously. The inversion is terminated once the data misfit falls below the tolerances η_{ϕ_d} defined in equation 10.

Because $\mathbf{m}_C^*[x = 0.33, y = 0.33]$ is a desirable model, we would like to be able to recover a similar solution in polar parameters ($\mathbf{m}_P^*[\rho = 0.47, \theta = 0.76]$). Unfortunately, as shown in Figure 5b, the minimization process performed in polar coordinates converges to a different solution ($\mathbf{m}_P[\rho = 0.67, \theta = 0.26]$) and the iterations steps are oscillatory. We display the equivalent iterations (the dashed red line) in the Cartesian space for comparison ($\mathbf{m}_C^P[x = 0.65, y = 0.17]$). This is an unsatisfactory solution.

Our main goal is to recover the solution $\mathbf{m}_P^*$, and we want to reach it with only a few model updates. To understand why the problem has arisen, we compare their respective gradients for a given starting model $\mathbf{m}_C^{(0)}$ and its equivalent polar model $\mathbf{m}_P^{(0)}$. In Cartesian coordinates, the gradient direction is

$$\mathbf{g}_C^{(0)} = \mathbf{F}_C^{\mathrm{T}} \mathbf{F}_C \mathbf{m}_C^{(0)} + \beta_C \mathbf{W}_C^{\mathrm{T}} \mathbf{W}_C \mathbf{m}_C^{(0)} - \mathbf{F}_C^{\mathrm{T}} \mathbf{d}^{\mathrm{obs}}. \tag{45}$$

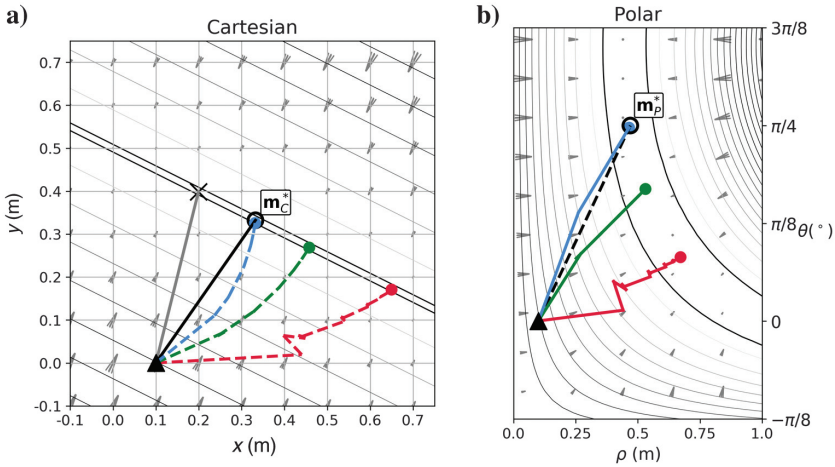

Figure 5. Contour maps for the objective functions of a two-parameter inverse problem solved in (a) Cartesian and (b) polar coordinate systems. The solid colored lines show the model updates taken by different algorithms in their respective coordinate systems and, in the dashed lines, the equivalent steps in the other domain for comparison. Each inversion started with the same initial model (triangle). The colors and inversions are gray, the nonweighted Cartesian problem; black, the sensitivity weighted Cartesian problem; red, the nonlinear polar coordinate system with fixed sensitivity weights; green, the polar problem with iterative sensitivity reweighting; and blue, with the added scaling to compensate for the dynamic range of the parameters (see equation 51).

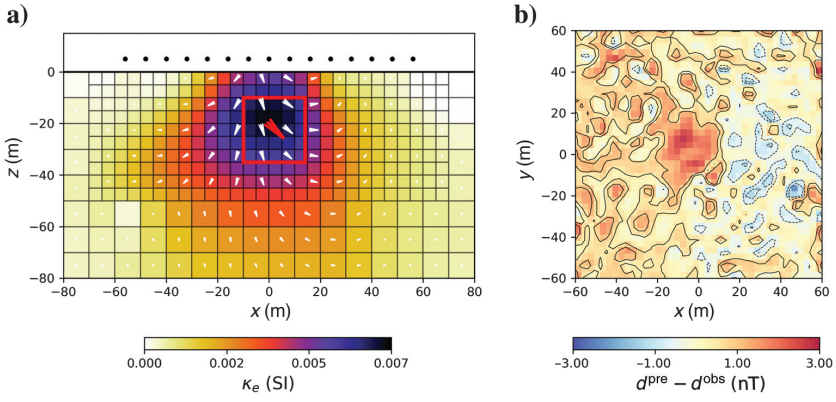

Figure 6. (a) Vertical section through the recovered magnetization vector model in spherical coordinates using sensitivity-based weighting and (b) the corresponding data residual map. The same poor starting model shown in Figure 4a was used, but the algorithm converged to a solution similar to the Cartesian solution.

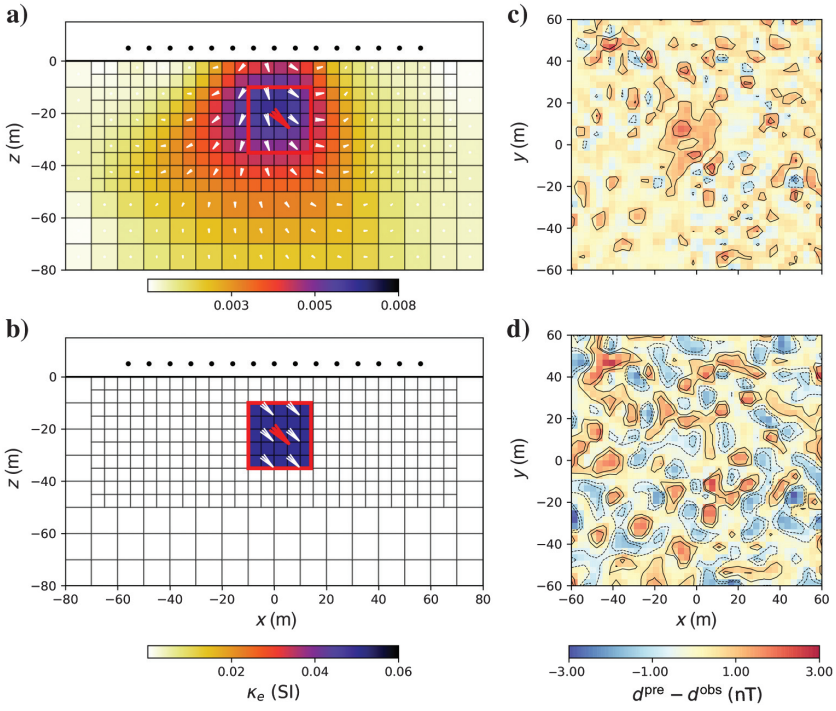

Figure 7. Vertical section through the recovered magnetization vector model in spherical coordinates using sensitivity-based weighting and the smooth Cartesian solution as starting model: (a) smooth regularization $(p_s = p_x = p_y = p_z = 2)$ and (b) sparse norms on the strength and angles of the magnetization vector $(p_s = p_x = p_y = p_z = 0)$. By using the sparse norms, we recover a solution that closely resembles the true model and, as observed in (d), we also eliminate the coherent signal in the residual data that is observed in (c).

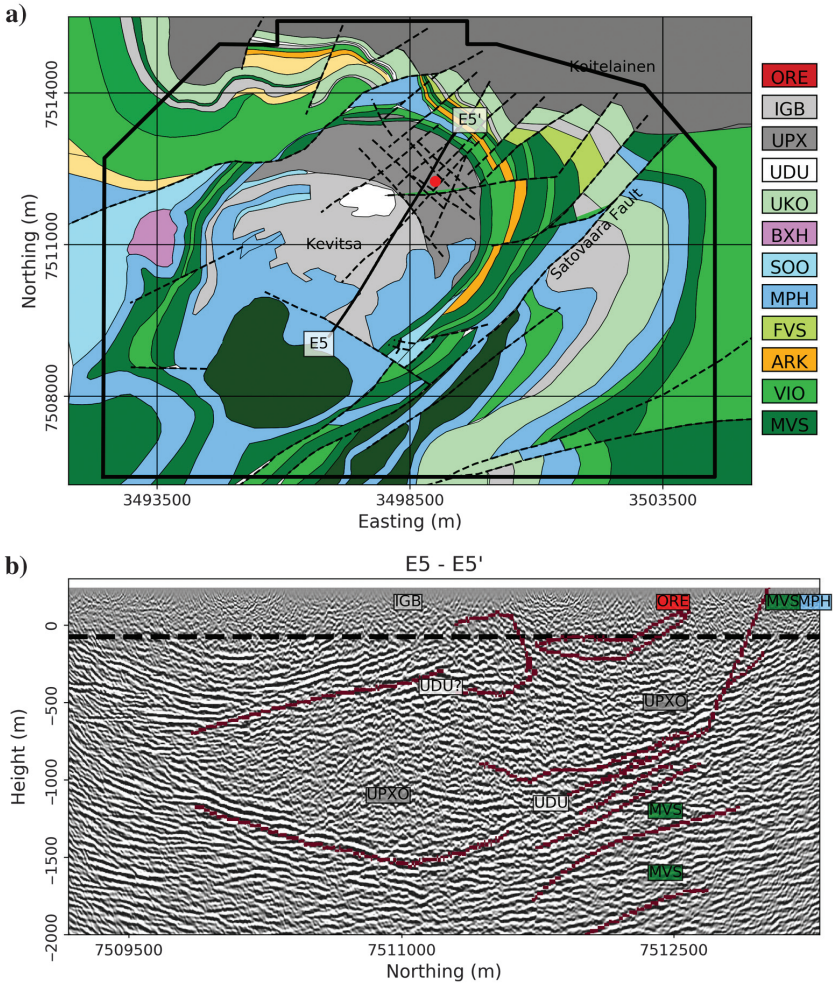

Figure 8. (a) Geologic map of the Kevitsa-Satovaara intrusive complex adapted from, with the geologic definition provided in Table 1. Mapped faults (dash) are shown for reference. (b) The 2D seismic line reflection line E5 with interpreted geologic contacts between the main reflectors.

We can convert these gradients to polar coordinate by multiplying equation 45 with the matrix of partial derivatives $\mathbf{S}$ such that

$$\mathbf{g}_P^C = \mathbf{S}^{\mathrm{T}}[\mathbf{F}_C^{\mathrm{T}}\mathbf{F}_C\mathbf{m}_C^{(0)} + \beta_C\mathbf{W}_C^{\mathrm{T}}\mathbf{W}_C\mathbf{m}_C^{(0)} - \mathbf{F}_C^{\mathrm{T}}\mathbf{d}^{\mathrm{obs}}]. \quad (46)$$

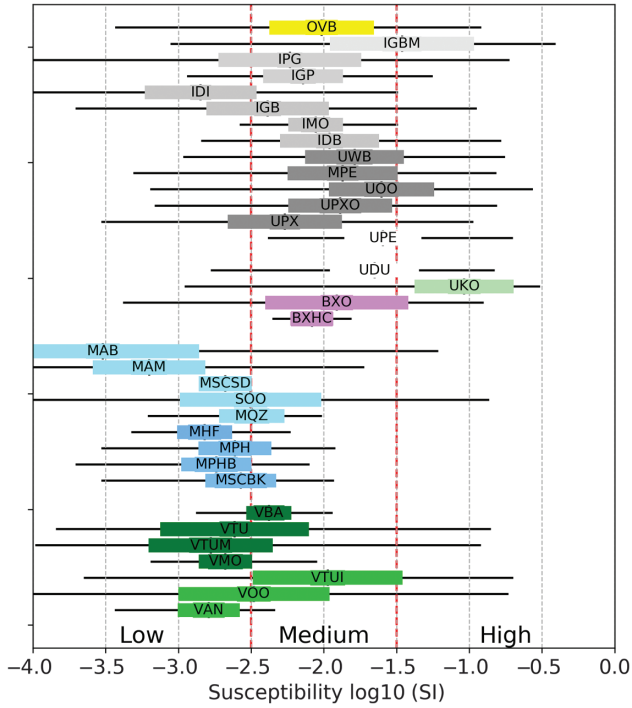

Figure 9. Whisker plot of magnetic susceptibility measured along 279 boreholes. The colored boxes have a width scaled by the calculated standard deviation and centered on the mean value for all intercepts belonging to the same lithologic classification, as defined in Table 1. The black lines on either side define the minimum and maximum values. The different lithologies are color coded and grouped based on their relative age and similarities in physical properties.

We want to compare this gradient to the gradient calculated in polar coordinates. From equation 44, and also keeping the same β_C used in the Cartesian framework, we have

$$\mathbf{g}_P = \mathbf{S}^{\mathrm{T}}\mathbf{F}_C^{\mathrm{T}}\mathbb{F}[\mathbf{m}_P^{(0)}] + \beta_C\mathbf{W}_C^{\mathrm{T}}\mathbf{W}_C\mathbf{m}_P^{(0)} - \mathbf{S}^{\mathrm{T}}\mathbf{F}_C^{\mathrm{T}}\mathbf{d}^{\mathrm{obs}}. \quad (47)$$

Noting that $\mathbf{F}_C\mathbf{m}_C^{(0)} = \mathbb{F}[\mathbf{m}_P^{(0)}]$ (i.e., the forward modelings are consistent), then equations 46 and 47 are the same only if

$$\mathbf{S}^{\mathrm{T}}\mathbf{W}_C^{\mathrm{T}}\mathbf{W}_C\mathbf{m}_C^{(0)} \simeq \mathbf{W}_C^{\mathrm{T}}\mathbf{W}_C\mathbf{m}_P^{(0)}. \quad (48)$$

We would like both sides to be roughly equal such that the gradient direction calculated in polar space resembles the gradient direction calculated in the Cartesian space. This is unlikely because $\mathbf{S}$ is a coordinate transformation matrix whose columns can have quite different values (see equation 43). The critical element is the specification of the regularization matrix for the polar system. Using the regularization matrix generated for the Cartesian system is inappropriate. Instead, we should use the sensitivity weighting for the polar problem. From equation 42, we had defined the polar sensitivities as $\mathbf{J} = \mathbf{F}_C\mathbf{S}$. We can define a new weighting matrix $\mathbf{W}_P$ by

$$\mathbf{W}_P = \mathrm{diag}\left[\left[\frac{\mathbf{w}_P}{\max(\mathbf{w}_P)}\right]^{1/2}\right], \quad w_{P_j} = \left[\sum_{i=1}^{N} J_{ij}^2\right]^{1/2}, \quad (49)$$

and our objective function to be minimized is

$$\phi(\mathbf{m}_P) = \|\mathbb{F}[\mathbf{m}_P] - \mathbf{d}^{\mathrm{obs}}\|_2^2 + \beta_P\|\mathbf{W}_P\mathbf{m}_P\|_2^2. \quad (50)$$

Importantly, we note that the sensitivities change at each iteration and so $\mathbf{W}_P$ must be continually updated. Inverting the nonlinear problem with the iterative scaling strategies (green), we recover the model $\mathbf{m}_P[\rho = 0.53, \theta = 0.53]$ (see Figure 5b). The solution has equal parameters of ρ and θ, and we reached this solution in a few iterations. In most applications, however, obtaining proportionality

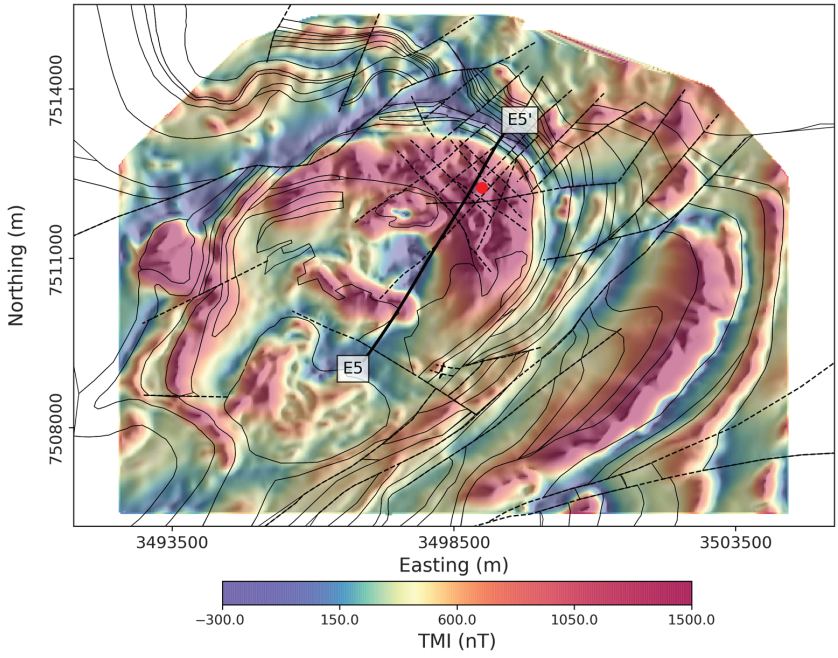

Figure 10. Observed TMI data over the Kevitsa intrusion with a histogram-equalized color scale. Geologic contacts (black), faults (dash) identified from surface mapping and the 2D seismic line locations E5, are shown for reference. Sun shading from the east is added to highlight subtle features (azimuth: 270° and dip: 45°).

between the magnitude and angle of the vector is not meaningful. Converted to Cartesian space $\mathbf{m}_C^P[x = 0.46, y = 0.27]$, we note that the solution is still different from $\mathbf{m}_C^*$.

To understand this result, we now examine equation 48 in terms of the size of the model parameters in $\mathbf{m}_P$. We have used a regularization function to penalize two parameters with different units: The radius $\rho \in [0, \infty]$ has units of length and angle $\theta \in [-\pi, \pi]$ is in radians. The range of values spanned by these parameters differs in scale as depicted by the aspect ratio of Figure 5b. Handling this disparity can be accomplished by introducing an additional weighting matrix that effectively scales the variables to the same dynamic range. We define a scaling factor between the two parameters

$$\omega = \frac{\|\boldsymbol{\rho}\|_\infty}{\|\boldsymbol{\theta}\|_\infty}. \tag{51}$$

In a general problem with lots of variables, we can evaluate $\|\boldsymbol{\rho}\|_\infty$ and $\|\boldsymbol{\theta}\|_\infty$ (the ratio of the largest model parameters at a given iteration). Here, where we have a restricted problem of two variables and one datum, we set this to the target ($\omega = \rho^*/\theta^*$). The scaled regularization becomes

$$\hat{\mathbf{W}}_P = \text{diag}([\,1 \quad \omega\,]^{(1/2)})\mathbf{W}_P. \tag{52}$$

The new scaled objective function becomes

$$\phi(\mathbf{m}_P) = \|\mathbb{F}[\mathbf{m}_P] - \mathbf{d}^{\text{obs}}\|_2^2 + \beta_P\|\hat{\mathbf{W}}_P\mathbf{m}_P\|_2^2. \tag{53}$$

Minimizing this function, we get the model (blue) presented in Figure 5 ($\mathbf{m}_P[\rho = 0.47, \theta = 0.74]$). Converted to Cartesian space, this solution $\mathbf{m}_C^P[x = 0.35, y = 0.32]$ closely matches $\mathbf{m}_C^*$.

Table 1. Intervals along boreholes KV200 and KV297 reporting significant remanent magnetization.

	Code	Description	Susceptibility
	OVB	Overburden	Medium
	IGB	IGB: Gabbro IPG: Pegmatite IGBO: Olivine gabbro IDI: Diorite IDB: Diabase IMO: Intrusive (mafic) IGBM: Magnetite gabbro	Medium High
	UPX	UPXO: Olivine peroxinite UOO: Ultramafic (Undiff.) MPE: Metaperidotite UWB: Websterite	Medium
	UDU	UDU: Dunite UPE: Peridotite	High
	UKO	Komatiite	High
	BXH	BXO (undiff.) BXHC: Hydrothermal (crackle)	Medium
	SOO	MAB: Albitite MAM: Amphibolite MQZ: Quartzite MSCSD: Schist	Low
	MPH	MPH: Phyllite MPHB: Black Phyllite MSCBK: Black Schist MHF: Hornfels	Low
	MVS	VMO: Volcanic Mafic VBA: Basalt VTUM: Volcanic tuff	Low
	VIO	VIO: Volcanic Intermediate VTUI: Volcanic tuff VAN: Andesite VOO: Volcanic (undiff.)	Medium

Table 2. Summary table grouping the various lithologic units logged from boreholes. The expected magnetic susceptibility contrasts are derived from Figure 9.

Hole ID	Interval (m)	κ (SI)	Inc. (°)	Q
KV297	0-52.9	0.034	−42.4	[2, 10]
KV200	29.9	0.038	−50.9	5.4

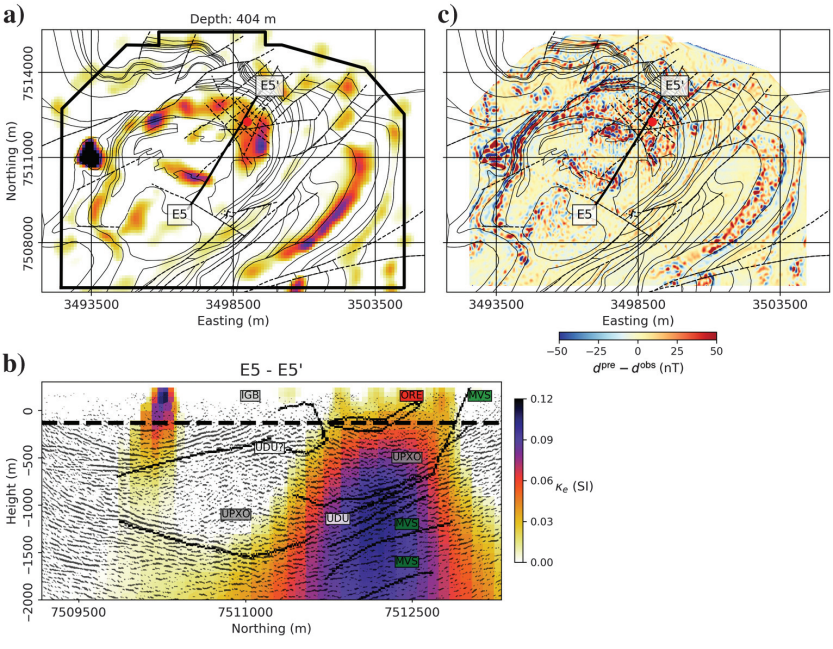

Figure 11. (a) Horizontal and (b) vertical sections through the recovered susceptibility model that ignores the effect of remanence. The identified lithologic contacts (black) are shown for reference. (c) The residual map shows a strong correlation with the negative magnetic data.

Scaled MVI-S algorithm

Now that we have demonstrated the benefit of an iterative sensitivity reweighting of the regularization, we revisit our synthetic magnetic problem. We invert the synthetic data once more with the starting magnetization orientated at 90° from the true model $\mathbf{m}_0(\rho = 10^{-2}, \theta = -45°, \phi = 0°)$. The recovered magnetization obtained after convergence of the scaled MVIS-S algorithm with smooth assumptions is presented in Figure 6a. We note close similarities with the MVI-C solution presented in Figure 3a, with the bulk magnetization centered around the position of the block. The inversion took 15 iterations to converge to this solution. This is a clear improvement over the model previously shown in Figure 4b.

From a practical standpoint, we have found that it is more efficient to initialize the MVI-S algorithm with the Cartesian solution. The linear MVI-C approach allows us to rapidly find a model that fits the observed data, and it provides a good starting point for the MVI-S formulation. We invert the data once more using the smooth Cartesian solution as a starting model. Figure 7a shows the recovered solution obtained after only three iterations of MVI-S. The solution closely resembles the starting Cartesian model. However, we note that there is some correlated signal in the residual misfit map in Figure 7c.

Having achieved a stable and reasonable solution with the ℓ_2-norm, we can now apply sparse norms to recover a block with a coherent magnetization direction. We vary the regularization measures on the amplitude, derivatives of amplitude, and derivatives of angles uniformly such that $(p_{i_s}, p_{i_x}, p_{i_y}\ p_{i_z} = 0)$. Figure 7b presents a section through the magnetic vector model. The shape of the anomalous body matches the magnetic block, and the magnetization direction is uniform and orientated at 45° inclination. In addition, the residual data map in Figure 7d shows almost no correlated signal. In previous inversions, we showed that the data could fit within the global tolerance $\phi_d \leq \phi_d^*$, but some of the important

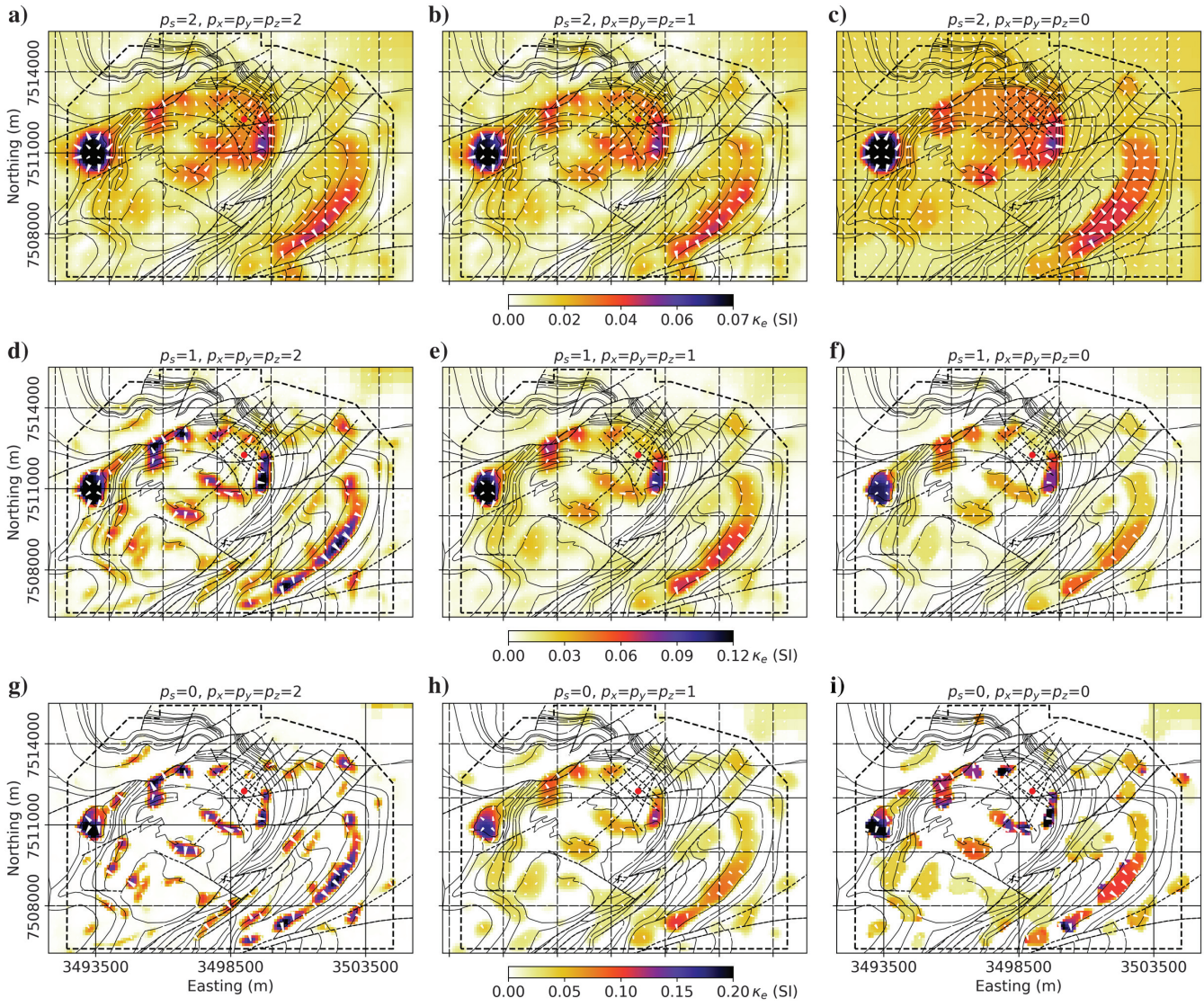

Figure 12. Horizontal sections at ≈300 m below the topography for a suite of models using various sparsity assumptions put on the amplitude of magnetization for p_s, $p_{x,y,z} \in [0, 2]$. Norm measures on the magnetization angle are fixed to $p_{x,y,z} = 0$ to promote uniform magnetization direction.

signal could not be replicated due to the smooth regularization. We have managed to better replicate the fields of a compact source by using the appropriate sparse and blocky assumptions. This result increases our confidence in our ability to accurately recover the magnetization of geologic bodies in three dimensions, as long as the regularization function is adaptable to the geologic settings.

CASE STUDY: KEVITSA NI-CU-PGE DEPOSIT

We demonstrate the capabilities of our inversion strategy with an airborne magnetic survey acquired over the Kevitsa Ni-Cu-PGE deposit, Northern Finland. The deposit was discovered in the mid-1980s through exploration programs sponsored by the Geological Survey of Finland. The geology of the deposit has been studied extensively over the past three decades by using surface mapping and borehole logging. Figure 8a presents a simplified geologic map of the Kevitsa-Satovaara intrusive complex, adapted from Koivisto et al. (2015). The Ni-Cu-PGE mineralization is hosted in a funnel shaped ultramafic olivine pyroxenite (UPXO) unit, bordered to the southwest by a gabbro (IGB) unit. The intrusion is hosted in a layered sequence of mafic volcanic (MVS) to intermediate volcanic (VIO) and carbonaceous phyllites (MPH) units. This sequence is interbedded with discontinuous layers of arkose (ARK), arenite (ARN), and felsic volcanic (FVS) units.

It is believed that the disseminated sulfide mineralization within the UPXO unit may have precipitated from the dissolution of Proterozoic Ni-Cu-PGE-rich MPH units and sulfur-rich evaporates (Mutanen, 1997). From seismic reflection surveys and borehole data, Koivisto et al. (2015) identify geologic contacts at a depth >1 km that defines the base of the intrusion (Figure 8b). A large dunite (UDU) block is located in the center of the intrusion. Thick lenses of dunite below the base of the Kevitsa intrusion were identified, as well as a vertical unit between the IGB and UPXO units. Although the extent and geometry of these UDU units are not well understood, we expect the dunite be serpentinized and hence highly magnetic. Table 1 provides a relative ranking of expected magnetization strength based upon the compilation of 105,000 susceptibility readings made on cores from 279 boreholes. Figure 9 summarizes the susceptibility measurements grouped by lithologies.

The deposit is interesting from a geophysical perspective due to the large amount of data that are acquired and made available to researchers: borehole petrophysical measurements, direct-current resistivity, magnetotelluric, ground gravity and magnetic data as well as two airborne time-domain electromagnetic surveys (VTEM 2009, SkyTEM 2010). In this study, we focus our efforts on the magnetic data collected during the 2009 VTEM survey, presented in Figure 10. The inducing field parameters at the time of acquisition were $B_0[A:52,800\ \text{nT}, I:77.5^\circ, D:12.2^\circ]$.

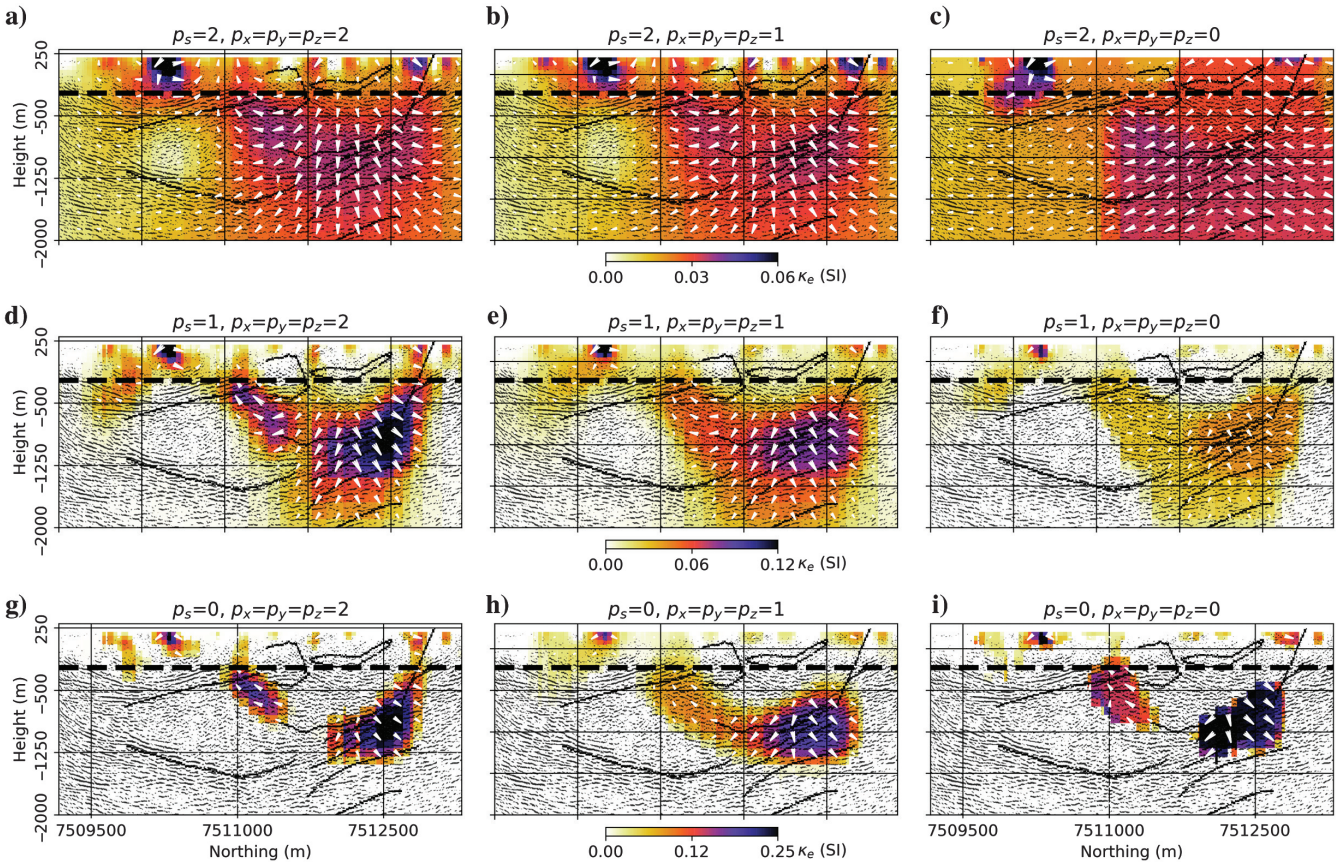

Figure 13. Vertical sections along the E5 seismic reflection line for a suite of models using various sparsity assumptions put on the amplitude of magnetization for p_s, $p_{x,y,z} \in [0, 2]$. Norm measures on the magnetization angle are fixed to $p_{x,y,z} = 0$ to promote a uniform magnetization direction.

From visual inspection, we note some obvious connections between the observed TMI data and the surface geology:

- strong magnetic signal correlated with the komatite (UKO), UPXO, and hydrothermal (BXH)
- moderate response from the MVS and VIO
- weak fields over most of the MPH units
- large negative anomaly within the UDU and near the southern edge of UPXO.

The strong negative field observed over the dunite unit within the UPXO is of particular interest for this study because it is likely related to remanent magnetization. Analysis of core samples indicates large Koenigsberger ratios and reversed magnetization direction in the UDU unit as summarized in Table 2 (Montonen, 2012, p. 47). It is important to note that large Koenigsberger ratios were also measured in the lower UPXO unit, although susceptibility values remained small. In the absence of an oriented core, no magnetic declinations were provided. From forward modeling of magnetized sheets, Montonen (2012) estimates that a magnetized unit with effective susceptibility of 0.82 SI and orientated $[I = -42.5°, D = 240°]$ could be responsible for the observed negative magnetic anomaly.

Magnetic susceptibility model

As a first pass, we invert the TMI data for a smooth susceptibility model ($p_s = p_x = p_y = p_z = 2$) and ignore the effects of remanence. To invert this large data set, we resort to a tiled octree mesh decoupling strategy (Haber and Schwartzbach, 2014). Sensitivity calculations are performed on nested submeshes to reduce the memory footprint required for the forward calculations. The dense sensitivity matrices are stored on disk in the zarr file format and accessed in parallel using the open-source Dask library (Dask, 2016). The combination of the forward mesh decoupling and lazy-loading of sensitivities allows us to run large problems on a desktop computer without the need for compression. The inversion algorithm is written under the open-source SimPEG package in Python (Cockett et al., 2015). More details regarding the algorithm are provided in Fournier (2019, p. 13). The full inversion domain comprises more than 500,000 cells and 17,000 data points.

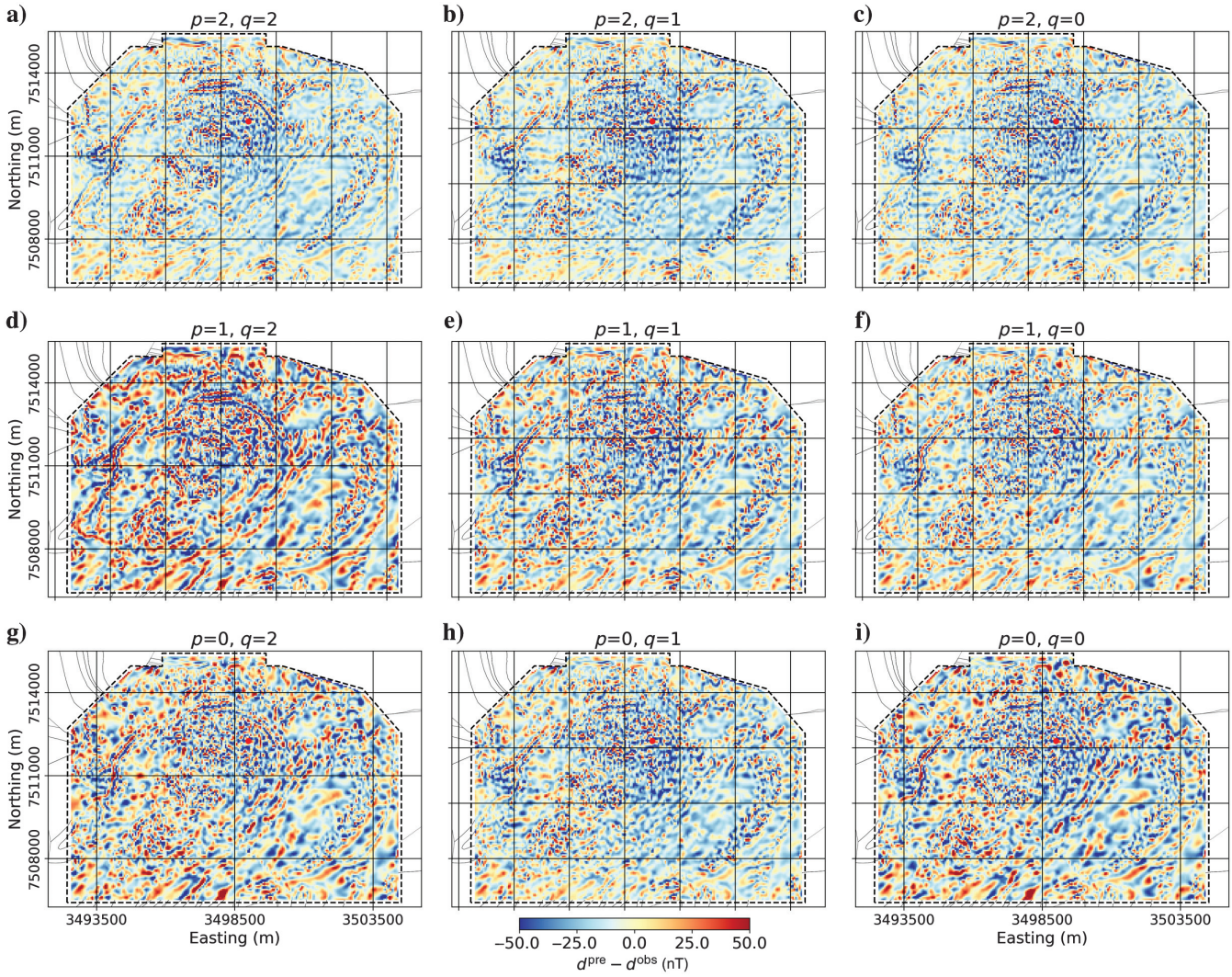

Figure 14. Residual data maps for the nine inversions shown in Figures 12 and 13.

From sections through the recovered susceptibility model, presented in Figure 11a and 11b, we note discrepancies with the known geology:

- In plan view, the arc shaped anomaly, southwest of the deposit, is recovered outside the mapped UKO unit.
- Along the E5 seismic section, no susceptibility anomaly is recovered over the central dunite. This directly contradicts the core sample measurements made by Montonen (2012).
- The shape and extent of the large anomaly correlate poorly with the UPXO unit interpreted by Koivisto et al. (2015) from seismic reflectors.

It is also important to note the large correlated residuals shown in Figure 11c. The inversion had difficulty finding a strictly positive susceptibility model that could account for the large positive and negative fields. This is a good indicator that the magnetic response observed at Kevitsa cannot solely be attributed to an induced magnetization alone.

Magnetization vector model

To address the issues posed by remanence, we proceed with the MVI-S algorithm. We perform a series of nine inversions with varying sparsity measures to assess the variability in the magnetization model. Starting from a common ℓ_2-norm MVI-C model, we sequentially vary the combination of norms applied to the amplitude and its derivatives for $(p_{\rho_x}, p_{\rho_{xyz}} \in [0, 2])$. In all cases, we fix the ℓ_p-norm regularization on the derivatives of the angles $(p_{\theta_{xyz}}, p_{\phi_{xyz}} = 0)$ to promote coherent magnetization orientations.

Horizontal and vertical sections through the recovered nine magnetization models are shown in Figures 12 and 13, respectively. The residual data maps presented in Figure 14 show variable data fit related to changes in assumptions carried by different regularization functions. To simplify the analysis, we superimpose the 90th percentile isovalue of amplitude for each of the nine models (Figure 15). We calculate an average magnetization direction (white) and standard deviation on the angle (red). We observe the following:

- Parts of the central dunite (UDU) unit appear to be reversely magnetized $[\kappa_e = 0.09$ SI, $I = -52° \pm 15°, D = 246° \pm 5°]$. The recovered inclination in the model cells nearest to the published results from Montonen (2012) agree well.
- A tabular magnetic anomaly between the IGB and UPX unit, likely related to the central dunite unit, appears to be plunging toward the southeast, potentially extending below the UPX unit as hypothesized by Koivisto et al. (2015).
- Strong magnetization recovered along the outershell of the UPX ultramafic intrusion appears to be pointing normal to its base.
- Similar radial outward magnetization recovered along the arc-shaped UKO unit, east of the Kevitsa deposit.

The last two remarks are interesting for a few reasons. First, strong magnetization near the base of the ultramafic supports the presence of magnetic UDU units below the intrusion. Second, the orientation of magnetization pointing radially outward may be indicative of past tectonic deformation. Under the assumption that the remanent magnetization component had been fairly uniform within the layered UDU, UKO, and UPX unit at the time of formation, then the current radiating magnetization pattern would be explained by subsequent folding of the units. If this is the case, then it would be one of the most complex geologic scenarios for which magnetic data inversions have been used to infer tectonic deformation.

Although our modeling of the central dunite unit agrees with published laboratory measurements, the cause for this reverse magnetization direction remains unclear. No other lithologic units appear to

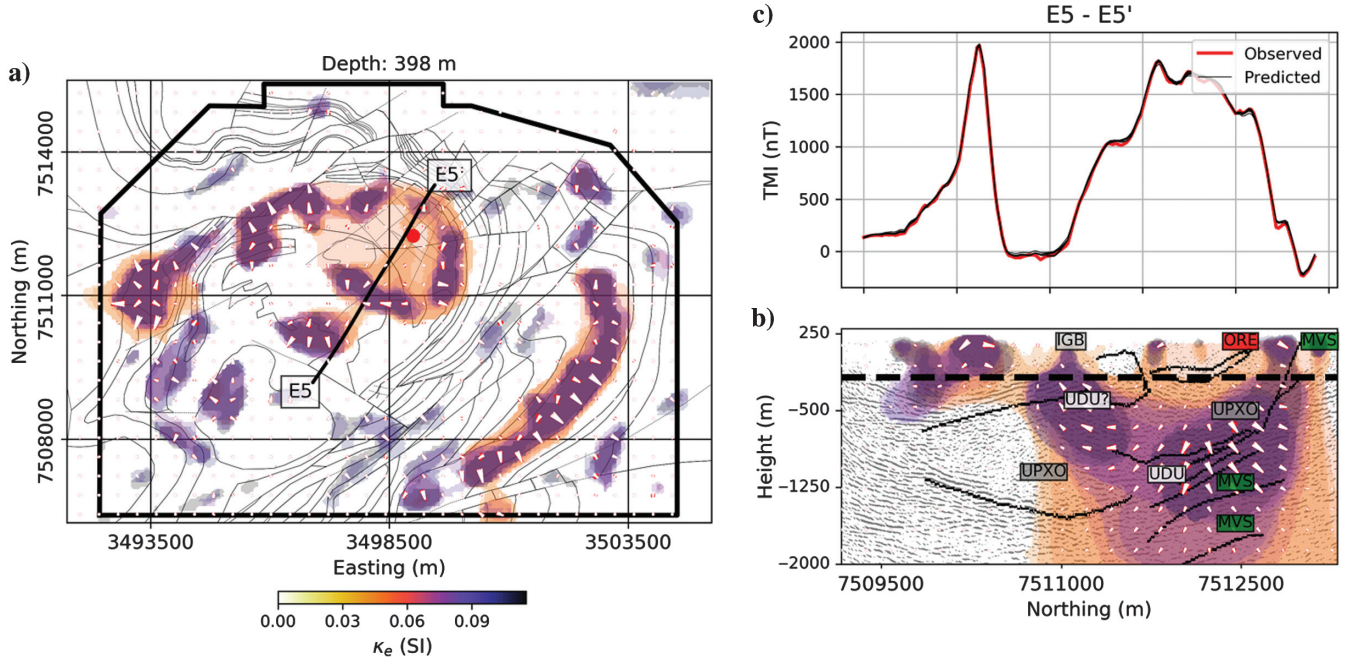

Figure 15. (a) Horizontal and (b) vertical sections through isocontours of magnetization recovered from nine mixed ℓ_p-norm inversions. Magnetization orientation (the white arrowheads) and standard deviation on the angle (the red arrowheads) are shown. (c) Data profile along the E5 section for the observed and predicted data calculated from the recovered models.

share this orientation. Remagnetization after emplacement of the ultramafic intrusion is unlikely because a similar reversed polarity pattern would also be expected elsewhere at Kevitsa. We speculate that the dunite block could be related to the lower UDU unit, which would have been folded to its current subvertical location.

CONCLUSION

In this study, we introduced an iterative sensitivity reweighting strategy to improve the convergence of the nonlinear MVI-S formulation. The iterative rescaling of the regularization function associated with the amplitude and angles of magnetization was crucial to achieve stable convergence of the algorithm. Smoother and more robust solutions allowed us to apply compact norms on the three model parameters independently, which greatly simplified the solution over the conventional MVI-C formulation. Despite this improvement, the MVI problem remains largely underdetermined. Incorporating a priori information, either through model constraints or joint physical properties, remains important to accurately represent the geology.

We demonstrated the capability of the newly accessible MVI-S formulation on an airborne magnetic survey collected over the Kevitsa Ni-Cu-PGE deposit. The recovered effective susceptibility and magnetization model confirmed that the central dunite unit was associated with strong reversed magnetization oriented roughly [$\kappa_e = 0.09$ SI, $I = -52° \pm 15°$, $D = 246° \pm 5°$]. Potentially the most significant outcome of this case study is the recovered sparse magnetization pointing normal to the base of the Kevitsa olivine-pyroxenite unit. If confirmed by laboratory measurements, this result would be one of the few paleomagnetic interpretations carried over folded geology that is based on the inversion of airborne magnetic data.

ACKNOWLEDGMENTS

The authors would like to thank M. Montonen at New Boliden for given us access to the geophysical data. Special thanks to E. Koivisto at the University of Helsinki for providing the 3D geologic surfaces and interpretation and F. Santaguida for providing the background information and putting us in contact with key people. Finally, we are grateful to the open-source community, in particular, those that contributed to the Dask and SimPEG packages.

DATA AND MATERIALS AVAILABILITY

Data associated with this research are available and can be obtained by contacting the corresponding author.

REFERENCES

Clark, D. A., 2014, Methods for determining remanent and total magnetisation of magnetic sources — A review: Exploration Geophysics, **45**, 271–304, doi: 10.1071/EG14013.

Cockett, R., S. Kang, L. J. Heagy, A. Pidlisecky, and D. W. Oldenburg, 2015, SimPEG: An open source framework for simulation and gradient based parameter estimation in geophysical applications: Computers and Geosciences, **85**, 142–154, doi: 10.1016/j.cageo.2015.09.015.

Dannemiller, N., and Y. Li, 2006, A new method for estimation of magnetization direction: Geophysics, **71**, no. 6, L69–L73, doi: 10.1190/1.2356116.

Dask, D. T., 2016, Dask: Library for dynamic task scheduling, https://dask.org, accessed 17 April 2019.

Ellis, R. G., B. de Wet, and I. N. Macleod, 2012, Inversion of magnetic data from remanent and induced sources: ASEG, Extended Abstracts, 1–4.

Enkin, R., 2003, Paleomagnetic analysis of selected Ekati kimberlite: Unpublished report for BHP Billiton Diamonds, Geological Survey of Canada.

Enkin, R. J., 2014, The rock physical property database of British Columbia, and the distinct petrophysical signature of the Chilcotin basalts: Canadian Journal of Earth Sciences, **51**, 327–338, doi: 10.1139/cjes-2013-0159.

Fedi, M., G. Florio, and A. Rapolla, 1994, A method to estimate the total magnetization direction from a distortion analysis of magnetic anomalies: Geophysical Prospecting, **42**, 261–274, doi: 10.1111/j.1365-2478.1994.tb00209.x.

Foss, C., and B. McKenzie, 2011, Inversion of anomalies due to remanent magnetisation: An example from the Black Hill Norite of South Australia: Australian Journal of Earth Sciences, **58**, 391–405, doi: 10.1080/08120099.2011.581310.

Fournier, D., 2015, A cooperative magnetic inversion method with lp-norm regularization: M.Sc. thesis, The University of British Columbia.

Fournier, D., 2019, Advanced potential field data inversion with lp-norm regularization: Ph.D. thesis, The University of British Columbia.

Fournier, D., and D. W. Oldenburg, 2019, Inversion using spatially variable mixed lp-norms: Geophysical Journal International, **218**, 268–282, doi: 10.1093/gji/ggz156.

Fullagar, P. K., and G. A. Pears, 2013, 3D magnetic modelling and inversion incorporating self-demagnetisation and interactions: ASEG, Extended Abstracts, 1–4.

Haber, C., and C. Schwartzbach, 2014, Parallel inversion of large-scale airborne time-domain electromagnetic data with multiple OcTree meshes: Inverse Problems, **30**, 055011, doi: 10.1088/0266-5611/30/5/055011.

Haber, E., D. W. Oldenburg, T. Farnocombe, and A. Cellar, 1997, Direct estimation of dynamic parameters in SPECT tomography: IEEE Transactions on Nuclear Science, **44**, 2425–2430, doi: 10.1109/23.656447.

Helbig, K., 1963, Some integrals of magnetic anomalies and their relation to the parameters of the disturbing body: Zeitschrift für Geophysik, **29**, 83–96.

Henkel, H., 1991, Petrophysical properties (density and magnetization) of rocks from the northern part of the Baltic Shield: Tectonophysics, **192**, 1–19, doi: 10.1016/0040-1951(91)90242-K.

Hestenes, M. R., and E. Stiefel, 1952, Method of conjugate gradient for solving linear systems: Journal of Research of the National Bureau of Standards, **49**, 409–436, doi: 10.6028/jres.049.044.

Kissel, C., and C. Laj, 1989, Paleomagnetic rotation and continental deformation: Kluwer Academic Publishers, Series C: Mathematical and Physical Sciences 254.

Koivisto, E., A. Malehmir, N. Hellqvist, T. Voipio, and C. Wijns, 2015, Building a 3D model of lithological contacts and near-mine structures in the Kevitsa mining and exploration site, Northern Finland: Constraints from 2D and 3D reflection seismic data: Geophysical Prospecting, **63**, 754–773, doi: 10.1111/1365-2478.12252.

Krahenbuhl, R. A., and Y. Li, 2007, Influence of self-demagnetization effect on data interpretation in strongly magnetic environments: 77th Annual International Meeting, SEG, Expanded Abstracts, 713–717, doi: 10.1190/1.2792514.

Kubota, R., and A. Uchiyama, 2005, Three-dimensional magnetization vector inversion of a seamount: Earth Planets Space, **57**, 691–699, doi: 10.1186/BF03351849.

Lelievre, P. G., and D. W. Oldenburg, 2009, A 3D total magnetization inversion applicable when significant, complicated remanence is present: Geophysics, **74**, no. 3, L21–L30, doi: 10.1190/1.3103249.

Li, Y., 2017, From susceptibility to magnetization: Advances in the 3D inversion of magnetic data in the presence of strong remanent magnetization: Presented at the 6th Decennial International Conference on Mineral Exploration.

Li, Y., A. Melo, C. Martinez, and J. Sun, 2019, Geology differentiation: A new frontier in quantitative geophysical interpretation in mineral exploration: The Leading Edge, **38**, 60–66, doi: 10.1190/tle38010060.1.

Li, Y., M. N. Nabighian, and D. Oldenburg, 2014, Using and equivalent source with positivity for low-latitude reduction to the pole without stration: Geophysics, **79**, no. 6, J81–J90, doi: 10.1190/geo2014-0134.1.

Li, Y., and D. W. Oldenburg, 1996, 3-D inversion of magnetic data: Geophysics, **61**, 394–408, doi: 10.1190/1.1443968.

Li, Y., S. E. Shearer, M. M. Haney, and N. Dannemiller, 2010, Comprehensive approaches to 3D inversion of magnetic data affected by remanent magnetization: Geophysics, **75**, no. 1, L1–L11, doi: 10.1190/1.3294766.

Li, Y., and J. Sun, 2016, 3-D magnetization inversion using fuzzy c-means clustering with application to geology differentiation: Geophysics, **81**, no. 5, J61–J78, doi: 10.1190/geo2015-0636.1.

Liu, S., X. Hu, Y. Xi, T. Liu, and S. Xu, 2015, 2D sequential inversion of total magnitude and total magnetic anomaly data affected by remanent magnetization: Geophysics, **80**, no. 3, K1–K12, doi: 10.1190/geo2014-0019.1.

Liu, S., X. Hu, H. Zhang, M. Geng, and B. Zuo, 2017, 3D magnetization vector inversion of magnetic data: Improving and comparing methods:

Pure and Applied Geophysics, **174**, 4421–4444, doi: 10.1007/s00024-017-1654-3.
Lockhart, G., H. Grutter, and J. Carlson, 2004, Temporal, geomagnetic and related attributes of kimberlite magmatism at Ekati, Northwest Territories, Canada: Lithos, **77**, 665–682, doi: 10.1016/j.lithos.2004.03.029.
Montonen, M., 2012, Induced and remanent magnetization in two boreholes of the Kevitsa intrusion: M.Sc. thesis, University of Helsinki.
Mutanen, T., 1997, Geology and ore petrology of the Akanvaara and Koitelainen mafic layered intrusions and the Keivitsa-Satovaara layered complex, northern Finland: Geological Survey of Finland 395.
Nocedal, J., and S. J. Wright, 1999, Numerical optimatization: Springer Science.
Norris, D. K., and R. F. Black, 1961, Application of paleomagnetism to thrust mechanics: Nature, **192**, 933–935, doi: 10.1038/192933a0.
Phillips, J. D., 2008, Can we estimate total magnetization directions from aeromagnetic data using Helbig's integrals?: Earth, Planets and Space, **57**, 681–689, doi: 10.1186/BF03351848.
Pilkington, M., 1997, 3-D magnetic imaging using conjugate gradients: Geophysics, **62**, 1132–1142, doi: 10.1190/1.1444214.
Pratt, D. A., B. K. McKenzie, and T. S. White, 2014, Remote remanence estimation (RRE): Exploration Geophysics, **45**, 314–323, doi: 10.1071/EG14031.
Pueyo, E. L., F. Cifelli, A. J. Sussman, and B. Oliva-Urcia, 2016, Introduction: Palaeomagnetism in fold and thrust belts: New perspective: Geological Society, London (Special Publications) 425.
Ramon, M. J., E. L. Pueyo, J. L. Briz, A. Pocovi, and J. C. Ciria, 2012, Flexural unfolding of horizon using paleomagnetic vectors: Journal of Structural Geology, **35**, 28–39, doi: 10.1016/j.jsg.2011.11.015.
Sharma, P. V., 1966, Rapid computation of magnetic anomalies and demagnetization effects caused by bodies of arbitrary shape: Pure Applied Geophysics, **64**, 89–109, doi: 10.1007/BF00875535.
Shearer, S., 2005, Three-dimensional inversion of magnetic data in the presence of remanent magnetization: M.Sc. thesis, Colorado School of Mines.
Tikhonov, A. N., V. Y. Arsenin, V. V. Stepanov, and A. G. Yagola, 1995, Numerical methods for the solution of ill-posed problems: Springer 328.
Vine, F. J., and D. H. Matthews, 1963, Magnetic anomalies over the oceanic ridges: Nature, **199**, 947–949, doi: 10.1038/199947a0.
Vogel, C. R., 2002, Computational methods for inverse problems (Frontiers in applied mathematics): Society for Industrial Mathematics.
Zhu, Y., M. S. Zhdanov, and M. Cuma, 2015, Inversion of TMI data for the magnetization vector using Gramian constraints: 85th Annual International Meeting, SEG, Expanded Abstracts, 1602–1606, doi: 10.1190/segam2015-5855046.1.